JCTC Journal of Chemical Theory and Computation

pubs.acs.org/JCTC Article

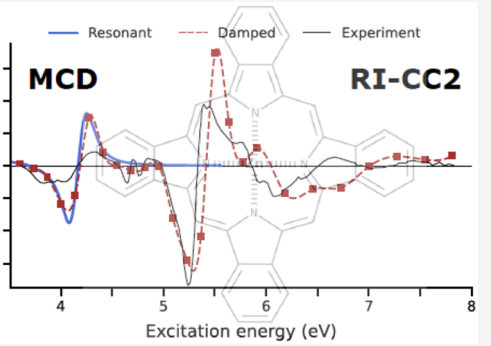
Efficient Protocol for Computing MCD Spectra in a Broad Frequency Range Combining Resonant and Damped CC2 Quadratic Response Theory

Josefine H. Andersen,* Sonia Coriani,* and Christof Hättig*

Cite This: J. Chem. Theory Comput. 2023, 19, 5977−5987 Read Online

ACCESS | Metrics & More | Article Recommendations | Supporting Information

ABSTRACT: Coupled cluster response theory offers a path to high-accuracy calculations of spectroscopic properties, such as magnetic circular dichroism (MCD). However, divergence or slow convergence issues are often encountered for electronic transitions in high-energy regions with a high density of states. This is here addressed for MCD by an implementation of damped quadratic response theory for resolution-of-identity coupled cluster singles-and-approximate-doubles (RI-CC2), along with an implementation of the MCD $\mathcal{A}$ term from resonant response theory. Combined, damped and resonant response theory calculations provide an efficient strategy to obtain MCD spectra over a broad frequency range and for systems that include highly symmetric molecules with degenerate excited states. The protocol is illustrated by application to zinc tetrabenzoporphyrin in the energy region of 2−8 eV and comparison to experimental data. Timings are reported for the resonant and damped approaches, showing that a greater part of the calculation time is consumed by the construction of the building blocks for the final MCD ellipticity. A recommendation on how to use the procedure is outlined.



Downloaded via BOCHUM LIBRARIES on October 9, 2023 at 12:26:39 (UTC).
See https://pubs.acs.org/sharingguidelines for options on how to legitimately share published articles.

1. INTRODUCTION

Magnetic circular dichroism (MCD) spectroscopy is a technique based on the measurement of the differential absorption of left and right circular polarized light passing through a sample immersed in a (relatively strong) magnetic field parallel to the direction of propagation of the light.[1] The frequency of the light is typically in a region of electronic absorption of the sample, that is, UV/vis, near IR, or X-ray,[1] but MCD of vibrational transitions can also be recorded.[2] A recently proposed experimental protocol utilizes pulsed vector beams, where the magnetic field generated by the vector beams replaces the external static field applied in conventional MCD experiments.[3] MCD has been applied with success to molecular systems to gain insight into structural, electronic, and magnetic properties, and experiments are moving into the investigation of nanosystems as well.[4]

Traditionally, the MCD signal is analyzed in terms of three characteristic band shapes, whose underlying electronic-structure intensity descriptors are known as the Faraday $\mathcal{A}$, $\mathcal{B}$, and C terms. The C term relates to the Zeeman splitting of degenerate ground states due to the external field, and its absorption-shaped band is temperature dependent. Only paramagnetic compounds exhibit C term signals.[1,5,6] $\mathcal{A}$ and $\mathcal{B}$ terms have different physical origins and are both independent of temperature. While the $\mathcal{A}$ term arises from the magnetic field-induced Zeeman splitting of degenerate electronic states, the $\mathcal{B}$ term is the result of mixing of nondegenerate states under the influence of the magnetic field. Thus, all molecules exhibit $\mathcal{B}$ -type signals while only molecules with a 3-fold or higher symmetry axis will have nonzero $\mathcal{A}$ terms.[1,5,6] A derivative line shape is indicative of the presence of an $\mathcal{A}$ term and, thus, excited-state degeneracy, while a transition with only a $\mathcal{B}$ term contribution gives rise to a Gaussian-shaped absorption feature. When present, the $\mathcal{A}$ term dominates the spectrum.[1,5,6]

MCD experiments can help to deconvolute bands observed in the regular absorption spectrum. Since the MCD signals take both positive and negative values, transitions can be better distinguished and, as mentioned, (near-)degenerate states can be identified from derivative lineshapes. In the interpretation of experimental MCD spectra, computational spectroscopy can provide valuable support. From quantum chemical calculation, it is possible to gain insight into the underlying electronic transitions, which in a spectrum are convoluted in a band of varying resolution. Among the most recent developments of theoretical approaches targeting MCD are implementations based on response theory[7] within the algebraic diagrammatic construction (ADC) scheme,[8] coupled cluster singles and

Received: May 22, 2023
Published: August 31, 2023



ACS Publications © 2023 American Chemical Society

https://doi.org/10.1021/acs.jctc.3c00536
J. Chem. Theory Comput. 2023, 19, 5977−5987

doubles (CCSD),[9] and resolution-of-identity coupled cluster singles and approximate doubles (RI-CC2),[10] as well as the linear-response (LR-) time-dependent (TD-) density functional theory (DFT) approach, in which excited states are calculated in a finite magnetic field.[11−13] Sun and Li[14] report a fully relativistic treatment of MCD incorporating spin−orbit effects, enabling the simulation of the C term and temperature dependence. Foglia et al.[15] present a computational approach to incorporate vibrational effects in the MCD spectra.

The calculation of the individual Faraday terms requires an explicit solution of the final excited states. This approach is limited by the convergence of the excited state eigenvectors and their derivatives, which becomes increasingly difficult in regions with a high density of states. Damped response theory and the complex polarization propagator framework offer an alternative approach where the spectrum is computed directly as an interpolation of cross-section grid points in any frequency region.[16−18] Implementations of this type of approach have been presented for various electronic-structure methods for the computation of linear spectroscopies such as one-photon absorption and electronic circular dichroism (ECD),[19−24] of C_6 dispersion coefficients,[25−27] and of the nonlinear spectroscopies such as MCD,[9,28] nuclear spin-induced circular dichroism (NSCD),[29] magneto-chiral dichroism (MChD) and magneto-chiral birefringence dispersion,[30] as well as resonant inelastic X-ray scattering (RIXS)[31−35] and two-photon absorption.[36−38]

In this work we extend the RI-CC2 framework for MCD spectroscopy[10] in TURBOMOLE[39] to include the calculation of the $\mathcal{A}$ term. Moreover, we address the shortcomings of the explicit calculation of the Faraday terms in regions where many close-lying electronic states can be expected by presenting an RI-CC2 implementation of a damped quadratic response. While the general derivation of both the resonant and damped approaches to MCD for CC response theory has been discussed in detail in ref 9, including numerical validation of their equivalence for CCSD, the RI-CC2 method allows for applications to molecular systems of sizes that are not amenable for CCSD and higher-order methods, while still producing reasonably accurate excitation energies and, thus, spectra.

Our protocol then combines the explicit calculation of individual $\mathcal{A}$ and $\mathcal{B}$ terms in regions of well-separated electronic transitions with damped response calculations of the MCD signal in dense spectral regions. This opens the possibility of investigating the MCD of molecules in a broad frequency range including cases with degenerate excited states. Furthermore, the implementation of the damped quadratic response can straightforwardly be extended to compute other perturbation-induced spectra such as NSCD and MChD.

To assess the time consumption of the resonant and damped pathways, we compare the timings for converging the equations and computing the MCD ellipticities for two degenerate resonant states and one complex frequency.

2. THEORY

For a randomly oriented sample in a static magnetic field placed along the z axis, the ellipticity of plane-polarized light passing through the sample parallel to the field can be determined as[40]

$$\theta = \frac{1}{6}\mu_0 c l N B_z \theta_{\mathrm{MCD}} \tag{1}$$

where μ_0 is the permeability, c is the velocity of light, l is the path length through the sample, N is the number density, and B_z is the strength of the external magnetic field along the z axis.

The MCD ellipticity, θ_{MCD}, can be computed by using different approaches. Within resonant (standard) response theory, the traditional expression for the MCD ellipticity of a system with a nondegenerate ground state takes the form (in atomic units)[9,40]

$$\theta_{\mathrm{MCD}} = -\omega \sum_j \left\{ \frac{\partial g(\omega_j, \omega)}{\partial \omega} \mathcal{A}(0 \to j) + g(\omega_j, \omega)\mathcal{B}(0 \to j) \right\} \tag{2}$$

where ω is the frequency of the incoming light, ω_j is the excitation energy of the electronic transition $0 \to j$, and $g(\omega_j, \omega)$ is a line shape function, e.g., a Gaussian or a Lorentzian. We refer to Section 3 for details on the type of line shape function applied in the present work.

The exact sum-overstates (SOS) representation of the $\mathcal{B}$ term is[41,42]

$$\mathcal{B}(0 \to j) = \varepsilon_{\alpha\beta\zeta}\mathrm{Im}\left[\sum_{k\neq 0} \frac{\langle k|m_\zeta|0\rangle}{\omega_k} \langle 0|\mu_\alpha|j\rangle\langle j|\mu_\beta|k\rangle + \sum_{k\notin\mathcal{D}_j} \frac{\langle j|m_\zeta|k\rangle}{\omega_k - \omega_j} \langle 0|\mu_\alpha|j\rangle\langle k|\mu_\beta|0\rangle \right] \tag{3}$$

where μ_α and m_α are Cartesian components of the electric dipole and magnetic dipole operators, respectively, and $\varepsilon_{\alpha\beta\zeta}$ is the Levi-Civita tensor. Implicit summations for α, β, and ζ are implied throughout. $\mathcal{D}_j$ is a set of degenerate states of which j is part ($j \in \mathcal{D}_j$). These degenerate states, if included in the sum over k, would make the second term of eq 3 diverge and are therefore explicitly excluded from the sum. The MCD signal of the $\mathcal{D}_j$ set is instead described via the nondivergent $\mathcal{A}$ term and the derivative of the line shape function (eq 2). Assuming a nondegenerate ground state, the exact SOS expression for the $\mathcal{A}$ term of an excited state j within the degenerate set $\mathcal{D}_j$ is[41,42]

$$\mathcal{A}(0 \to j) = \frac{1}{2}\varepsilon_{\alpha\beta\zeta}\mathrm{Im} \sum_{\substack{j'\in\mathcal{D}_j \\ j'\neq j}} \langle 0|\mu_\alpha|j\rangle\langle j|m_\zeta|j'\rangle\langle j'|\mu_\beta|0\rangle \tag{4}$$

which can be recognized as the residue of the dispersive term of eq 3 in the limit of $(\omega_k - \omega_j) \to 0$.

In general, computing the Faraday terms from their SOS expressions is highly inefficient. Instead, the $\mathcal{A}$ and $\mathcal{B}$ terms can be obtained, e.g., from the double and single residues of appropriate quadratic response functions,[40,43] or from the magnetic field-derivatives of the excitation energy and the one-photon dipole transition strength.[44−46]

2.1. Implementation of the Faraday $\mathcal{A}$ and $\mathcal{B}$ Terms. In the work of Faber et al.,[9] the expression for the MCD $\mathcal{A}$ term within CC theory was derived from a residue analysis of the magnetic field-derivative of the dipole−dipole transition strength. Following this derivation, we calculate the $\mathcal{A}$ term as

$$\mathcal{A}(0 \to j) = -\frac{1}{4}\varepsilon_{\alpha\beta\zeta}\mathrm{Im} \sum_{\substack{j'\in\mathcal{D}_j \\ j'\neq j}} \left(T^{\mu_\alpha}_{0j'} T^{m_\zeta}_{j'j} T^{\mu_\beta}_{j0} + T^{\mu_\alpha}_{0j} T^{m_\zeta}_{jj'} T^{\mu_\beta}_{j'0}\right) \tag{5}$$

$T^{\mu_\alpha}_{0j}$ and $T^{\mu_\beta}_{j0}$ are the CC one-photon dipole transition moments, whose computation has been discussed several times elsewhere, see, e.g., refs 7 and 9. In general, the one-photon transition moment for the magnetic dipole operator m_ζ between the degenerate states j and j', $T^{m_\zeta}_{jj'}$, can be expressed in two ways,[7]

https://doi.org/10.1021/acs.jctc.3c00536
J. Chem. Theory Comput. 2023, 19, 5977−5987

$$T_{jj'}^{m_\zeta} = \bar{E}_j(-\omega_j)(\mathbf{A}^{m_\zeta} + \mathbf{B}t^{m_\zeta}(0))E_{j'}(\omega_{j'}) \tag{6}$$

or

$$T_{jj'}^{m_\zeta} = \bar{E}_j(-\omega_j)\mathbf{A}^{m_\zeta}E_{j'}(\omega_{j'}) + \bar{N}_{jj'}(\omega_j, \omega_{j'})\xi^{m_\zeta} \tag{7}$$

where the multipliers $\bar{N}_{jj'}$ are determined by solving the linear equation[7]

$$\bar{N}_{jj'}(-\omega_j, \omega_{j'})(\mathbf{A} + (\omega_j - \omega_{j'})\mathbf{1}) = -\bar{E}_j(-\omega_j)\,\mathbf{B}\,E_{j'}(\omega_{j'}) \tag{8}$$

In the equations above, $\bar{E}_j(-\omega_j)$ and $E_j(\omega_j)$ are the left and right eigenvectors of the excited state j, obtained by solving the CC eigenvalue equations

$$\mathbf{A}E_j(\omega_j) = \omega_j E_j(\omega_j) \qquad \text{and} \qquad \bar{E}_j(-\omega_j)\mathbf{A} = \omega_j\bar{E}_j(-\omega_j) \tag{9}$$

The CC Jacobian matrix, $\mathbf{A}$, as well as the matrices $\mathbf{A}^m$ and $\mathbf{B}$ are partial derivatives of the CC Lagrangian,[7] and we refer to Table S1 in the SI for a summary of the CC building blocks. Additional definitions can be found in refs 7, 9, and 44.

In order to apply eq 6, one must solve for the response amplitudes t^{m_ζ} at zero frequency, whereas solving for the $\bar{N}_{jj'}$ multipliers is necessary for eq 7. Since the $t^{m_\zeta}(0)$ vectors are also involved in the calculation of the $\mathcal{B}$ term (and do not scale with the number of excited states), it is advantageous to use eq 6 to obtain the MCD $\mathcal{A}$ term. Details on the implementation of the contractions needed to evaluate the above quantities for RI-CC2 in TURBOMOLE can be found in refs 47 and 48.

Continuing to follow the derivations for CC methods of ref 9, the $\mathcal{B}$ term is calculated as

$$\mathcal{B}(0 \to j) = -\frac{1}{2}\varepsilon_{\alpha\beta\zeta}\mathrm{Im}({}^{\perp}T_{0j}^{\mu_\alpha m_\zeta}T_{j0}^{\mu_\beta} + T_{0j}^{\mu_\alpha}{}^{\perp}T_{j0}^{\mu_\beta m_\zeta}) \tag{10}$$

${}^{\perp}T_{0j}^{\mu_\alpha m_\zeta}$ and ${}^{\perp}T_{j0}^{\mu_\beta m_\zeta}$ are the (right and left) magnetic field-derivatives of the one-photon dipole transition moments[44]

$$\begin{aligned}{}^{\perp}T_{0j}^{\mu_\alpha m_\zeta} = \left.\frac{\mathrm{d}T_{0j}^{\mu_\alpha}}{\mathrm{d}B_\zeta}\right|_{\mathbf{B}=\mathbf{0}} &= [\mathbf{G}t^{m_\zeta}(0)t^{\mu_\alpha}(-\omega_j) \\ &+ \mathbf{F}^{m_\zeta}t^{\mu_\alpha}(-\omega_j) + \mathbf{F}^{\mu_\alpha}t^{m_\zeta}(0)]E_j(\omega_j) \\ &+ \bar{M}_j(\omega_j)[\mathbf{A}^{\mu_\alpha}t^{m_\zeta}(0) + \mathbf{A}^{m_\zeta}t^{\mu_\alpha}(-\omega_j) \\ &+ \mathbf{B}t^{m_\zeta}(0)t^{\mu_\alpha}(-\omega_j)] + \omega_j^{m_\zeta}[\bar{M}_j(\omega_j)t^{\mu_\alpha}(-\omega_j)] \\ &+ \bar{\xi}^{\mu_\alpha}(-\omega_j){}^{\perp}E_j^{m_\zeta}(\omega_j, 0) + \bar{\xi}^{m_\zeta}(0)E_j^{\mu_\alpha}(\omega_j, -\omega_j)\end{aligned} \tag{11}$$

and

$${}^{\perp}T_{j0}^{\mu_\alpha m_\zeta} = \frac{\mathrm{d}T_{j0}^{\mu_\alpha}}{\mathrm{d}B_\zeta} = {}^{\perp}\bar{E}_j^{m_\zeta}(-\omega_j, 0)\xi^{\mu_\alpha} + \bar{E}_j(-\omega_j)\mathbf{A}^{\mu_\alpha}t^{m_\zeta}(0) \tag{12}$$

As before, we refer to refs 7, 9, and 49 for definitions of most of CC building blocks and only draw attention to some of the relevant quantities for our discussion.

The term in eq 11 involving $\omega_j^{m_\zeta}$ (i.e., the derivative of the excitation energy with respect to the magnetic field) is only nonzero for a degenerate j, since $\omega_j^{m_\zeta}$ corresponds to the definition of the excited-state expectation value $T_{jj}^{m_\zeta}$ of the imaginary angular momentum operator.

The first-order responses of the eigenvectors are determined according to[9,10,44]

$$[\mathbf{A} - (\omega_j - \omega_j)\mathbf{1}]E_j^{\mu_\alpha}(\omega_j, -\omega_j) = [\mathbf{A}^{\mu_\alpha} + \mathbf{B}t^{\mu_\alpha}(-\omega_j)]E_j(\omega_j) \tag{13}$$

$$\begin{aligned}&(P_j[\mathbf{A} - (\omega_j + 0)\mathbf{1}]P_j)^{\perp}E_j^{m_\zeta}(\omega_j, 0) \\ &\quad = -P_j[\mathbf{A}^{m_\zeta} + \mathbf{B}t^{m_\zeta}(0)]E_j(\omega_j)\end{aligned} \tag{14}$$

$$\begin{aligned}&{}^{\perp}\bar{E}_j^{m_\zeta}(-\omega_j, 0)(P_j[\mathbf{A} + (0 - \omega_j)\mathbf{1}]P_j) \\ &\quad = -\bar{E}_j(-\omega_j)[\mathbf{A}^{m_\zeta} + \mathbf{B}t^{m_\zeta}(0)]P_j\end{aligned} \tag{15}$$

The projector P_j removes singularities in the responses of the eigenvectors to the magnetic field (${}^{\perp}\bar{E}_j^{m_\zeta}$ and ${}^{\perp}E_j^{m_\zeta}$) by projecting onto the orthogonal complement of the undifferentiated eigenvectors,[9,10] as indicated by the $\perp$ superscript:

$${}^{\perp}\bar{E}_j^{m_\zeta} = P_j\bar{E}_j^{m_\zeta} \tag{16}$$

$${}^{\perp}\bar{E}_j^{m_\zeta} = \bar{E}_j^{m_\zeta}P_j \tag{17}$$

Generalized for a degenerate state j, P_j takes the form of the outer product of the eigenvectors summed over the set $\mathcal{D}_j$:

$$P_j = 1 - \sum_{j' \in \mathcal{D}_j} E_{j'} \otimes \bar{E}_{j'} \tag{18}$$

In the case where j is not degenerate, $\mathcal{D}_j$ is simply of size 1.

The implementation of the MCD $\mathcal{B}$ term for nondegenerate cases and of the derivative transition moments for RI-CC2 in TURBOMOLE have been reported in refs 10 and 50, respectively. This has now been generalized for degenerate states by adding the $\omega_j^{m_\zeta}[\bar{M}_j(\omega_j)t^{\mu_\alpha}(-\omega_j)]$ contribution to $\mathcal{B}(0 \to j)$ for $j \in \mathcal{D}_j$, and by keeping the magnetic field-derivatives of the eigenvector of state j orthogonal to the entire set $\mathcal{D}_j$ according to eq 18. The calculation of the $\mathcal{A}$ term has also been added, together with an automated procedure to detect degeneracies.

Thus, in resonant response theory, the $\mathcal{A}$ and $\mathcal{B}$ terms are computed separately for each individual excited state and the ellipticity is put together according to eq 2.

2.2. Implementation of the Quadratic Response Function. Alternative to the resonant approach, one can obtain the MCD ellipticity from damped response theory, either as the real part of the dipole−dipole-magnetic dipole damped quadratic response function[28,40]

$$\theta_{\mathrm{MCD}} = -\omega\varepsilon_{\alpha\beta\zeta}\mathrm{Re}\langle\langle\mu_\alpha; \mu_\beta, m_\zeta\rangle\rangle_{\omega+i\gamma,0} \tag{19}$$

or, equivalently, as the magnetic field-derivative of the damped dynamic polarizability[9]

$$\theta_{\mathrm{MCD}} = -\omega\varepsilon_{\alpha\beta\zeta}\mathrm{Re}\left(\frac{\mathrm{d}\langle\langle\mu_\alpha; \mu_\beta\rangle\rangle_{\omega+i\gamma}}{\mathrm{d}B_\zeta}\right)_{\mathbf{B}=\mathbf{0}} \tag{20}$$

The final working equations are the same.

In damped response theory, a finite lifetime of the electronically excited states is implemented by introducing a complex excitation energy. The generalization of standard to damped response theory is effectively carried out by making the replacement[16−18]

https://doi.org/10.1021/acs.jctc.3c00536
J. Chem. Theory Comput. 2023, 19, 5977−5987

$$\omega \rightarrow \omega + i\gamma \tag{21}$$

for all frequency-dependent components of the response functions. The damping factor γ is the inverse lifetime and takes an empirical value. Contributions from both the $\mathcal{A}$ and $\mathcal{B}$ terms are contained within the damped response function,[51] where also the band profiles are built into the formula in the form of Lorentzian broadening functions.[17,52]

Within CC theory, the quadratic response function[7] can be expressed as

$$\begin{aligned}\langle\langle A;\, B,\, C\rangle\rangle_{\overline{\omega}_B,\overline{\omega}_C} = \frac{1}{2}\hat{C}^{\pm\omega}\Big[&\mathbf{G}t^A(\overline{\omega}_A)t^B(\overline{\omega}_B)t^C(\overline{\omega}_C)\\ &+ \frac{1}{2}\hat{P}^{ABC}\overline{t}^A(\overline{\omega}_A)\mathbf{B}t^B(\overline{\omega}_B)t^C(\overline{\omega}_C)\\ &+ \frac{1}{2}\hat{P}^{ABC}\mathbf{F}^A t^B(\overline{\omega}_B)t^C(\overline{\omega}_C)\\ &+ \hat{P}^{ABC}\overline{t}^A(\overline{\omega}_A)\mathbf{A}^B t^C(\overline{\omega}_C)\Big]\end{aligned} \tag{22}$$

where $\overline{\omega}_A = -\overline{\omega}_B - \overline{\omega}_C$, the permutation operator $\hat{P}^{ABC}$ symmetrizes with respect to permutations of the operators A, B, and C together with the accompanied frequencies, and $\hat{C}^{\pm\omega}$ symmetrizes with respect to a change of sign of the real parts of the frequencies (denoted by ω_A, ω_B, and ω_C) followed by complex conjugation. While $\overline{\omega}_C$ is assumed to be real, the frequencies $\overline{\omega}_A$ and $\overline{\omega}_B$ can be either real or complex. In the former case, the quadratic response function is purely real or purely imaginary (depending on the combination of A, B, and C), and the building blocks are computed according to standard response theory. An example of an observable that can be calculated from the standard formulation of the quadratic response function with real frequencies is the ground state hyperpolarizability. For the case that $\overline{\omega}_A$ and $\overline{\omega}_B$, on the other hand, are complex, we allow the replacement of eq 21 and the response function becomes complex, i.e., damped. It follows that the implementation of the damped quadratic response function in eq 19 is a (conceptually) simple generalization of the implementation for real frequencies.

To compute the MCD ellipticity from the damped quadratic response function according to eq 19 the frequencies are set to $\overline{\omega}_B = \omega + i\gamma$ and $\overline{\omega}_C = 0$, and we thus need both damped response amplitudes and damped response multipliers. In other words, we must solve the right and left linear response equations for the dipole moment operator with complex frequencies, i.e.,

$$[\mathbf{A} - (\omega + i\gamma)\mathbf{1}]t^\mu(\omega + i\gamma) = -\xi^\mu \tag{23}$$

$$\begin{aligned}&\overline{t}^\mu(-\omega - i\gamma)[\mathbf{A} - (\omega + i\gamma)\mathbf{1}]\\ &\quad = -\eta^\mu - \mathbf{F}t^\mu(-\omega - i\gamma) \equiv -\overline{\xi}^\mu(-\omega - i\gamma)\end{aligned} \tag{24}$$

In the RI-CC2 implementation in TURBOMOLE, the above response equations are effectively solved only in the space of single excitations; i.e., only the singles components of all vectors are explicitly computed and stored; contributions from the doubles are computed on-the-fly. The derivation and implementation of eq 23 for (RI-)CC2 in TURBOMOLE are described in detail in the work by Fedotov et al.[19] It boils down to iteratively solving the effective linear CC2 response equations for the singles amplitudes

$$\begin{bmatrix}\mathbf{A}_{SS}^{\text{eff}} - \omega\mathbf{1}_{SS} & -\mathbf{\Gamma}_{SS}^{\text{eff}} + \gamma\mathbf{1}_{SS}\\ \mathbf{\Gamma}_{SS}^{\text{eff}} - \gamma\mathbf{1}_{SS} & \mathbf{A}_{SS}^{\text{eff}} - \omega\mathbf{1}_{SS}\end{bmatrix}\begin{bmatrix}t_{R,S}^\mu\\ t_{I,S}^\mu\end{bmatrix} = -\begin{bmatrix}\xi_{R,S}^{\mu,\text{eff}}\\ \xi_{I,S}^{\mu,\text{eff}}\end{bmatrix} \tag{25}$$

where the ω- and γ-dependent effective matrices are defined as

$$\mathbf{A}_{SS}^{\text{eff}}(\omega,\gamma) = \mathbf{A}_{SS} - \mathbf{A}_{SD}\frac{\Delta}{\Delta^2 + \gamma^2}\mathbf{A}_{DS} \tag{26a}$$

$$\mathbf{\Gamma}_{SS}^{\text{eff}}(\omega,\gamma) = -\mathbf{A}_{SD}\frac{\gamma}{\Delta^2 + \gamma^2}\mathbf{A}_{DS} \tag{26b}$$

with the diagonal matrix $\mathbf{\Delta} = \mathbf{A}_{DD} - \omega\mathbf{1}_{DD}$ and the effective right-hand sides (RHS)

$$\xi_{R,S}^{\mu,\text{eff}}(\omega,\gamma) = \xi_{R,S}^\mu - \mathbf{A}_{SD}\frac{\Delta}{\Delta^2 + \gamma^2}\xi_{R,D}^\mu + \mathbf{A}_{SD}\frac{\gamma}{\Delta^2 + \gamma^2}\xi_{I,D}^\mu \tag{27a}$$

$$\xi_{I,S}^{\mu,\text{eff}}(\omega,\gamma) = \xi_{I,S}^\mu - \mathbf{A}_{SD}\frac{\Delta}{\Delta^2 + \gamma^2}\xi_{I,D}^\mu - \mathbf{A}_{SD}\frac{\gamma}{\Delta^2 + \gamma^2}\xi_{R,D}^\mu \tag{27b}$$

Above and in the following, indices R and I label the real and imaginary component of the given vectors (e.g., $t = t_R + it_I$), and subscripts S and D refer to the single and double spaces, respectively.

The corresponding derivation of the (RI-)CC2 response multiplier equations for complex frequencies, eq 24, is discussed in detail in Section S5 in the SI. In compact matrix form, the effective damped CC2 multiplier equations of eq 24 become

$$\begin{aligned}&[\overline{t}_{R,S}^\mu \quad \overline{t}_{I,S}^\mu]\begin{bmatrix}\mathbf{A}_{SS}^{\text{eff}} - \omega\mathbf{1}_{SS} & \mathbf{\Gamma}_{SS}^{\text{eff}} - \gamma\mathbf{1}_{SS}\\ -\mathbf{\Gamma}_{SS}^{\text{eff}} + \gamma\mathbf{1}_{SS} & \mathbf{A}_{SS}^{\text{eff}} - \omega\mathbf{1}_{SS}\end{bmatrix}\\ &\quad = -\begin{bmatrix}\overline{\xi}_{R,S}^{\mu,\text{eff}} & \overline{\xi}_{I,S}^{\mu,\text{eff}}\end{bmatrix}\end{aligned} \tag{28}$$

and the effective RHSs take the form

$$\overline{\xi}_{R,S}^{\mu,\text{eff}} = \overline{\xi}_{R,S}^\mu - \overline{\xi}_{R,D}^\mu\frac{\Delta}{\Delta^2 + \gamma^2}\mathbf{A}_{DS} + \overline{\xi}_{I,D}^\mu\frac{\gamma}{\Delta^2 + \gamma^2}\mathbf{A}_{DS} \tag{29a}$$

$$\overline{\xi}_{I,S}^{\mu,\text{eff}} = \overline{\xi}_{I,S}^\mu - \overline{\xi}_{I,D}^\mu\frac{\Delta}{\Delta^2 + \gamma^2}\mathbf{A}_{DS} - \overline{\xi}_{R,D}^\mu\frac{\gamma}{\Delta^2 + \gamma^2}\mathbf{A}_{DS} \tag{29b}$$

Note that, in connection with the current work, the convergence of the iterative solution of the CC2 response equations has been improved by determining the coefficients for the expansion of the solution vectors on the basis of the trial vectors by the requirement that the residual in the full space is minimized, instead of solving (as otherwise described in ref 19) the equations projected to the subspace of trial vectors. For further details, we refer to Section S6 in the SI.

After computation of the complex response amplitudes and multipliers via eqs 23 and 24, the damped response function for MCD is constructed. The first term of eq 22 is the contractions of three response vectors with the $\mathbf{G}$ matrix: $\mathbf{G}t^{\mu_\alpha}(\omega + i\gamma)t^{\mu_\beta}(-\omega - i\gamma)t^{m_\zeta}(0)$. For details on the implementation of the $\mathbf{G}$-matrix contractions, see Section S7 in the SI. The contraction of the $\mathbf{B}$ matrix with one (complex) vector from the left and two from the right in the second term of eq 22 is evaluated analogously to the $\mathbf{F}$-matrix contractions described in ref 53. There, the singles components of an intermediate

https://doi.org/10.1021/acs.jctc.3c00536
J. Chem. Theory Comput. 2023, 19, 5977−5987

$\sigma(\overline{t}^A, t^B)$ are contracted with the singles components of the t^C amplitudes, whereas the contraction of the doubles is evaluated directly from the intermediates for constructing $\sigma(\overline{t}^A, t^B)_D$, thereby avoiding the storage of any doubles intermediates. For the **B**-matrix contractions, the unperturbed Lagrange multipliers are replaced by response multipliers, and a contribution that originates from the projection onto the Hartree−Fock state is skipped.

The last two terms of eq 22 are rewritten as contractions between complex perturbed one-particle densities and one-electron integrals:[53]

$$\mathbf{F}^{\mu_\alpha t^{\mu_\beta}}(-\omega - i\gamma)t^{m_\zeta}(0) = \hat{h}^{\mu_\alpha} D^F(t^{\mu_\beta}, t^{m_\zeta}) \tag{30}$$

$$\overline{t}^{\mu_\alpha}(\omega + i\gamma)\mathbf{A}^{\mu_\beta t^{m_\zeta}}(0) = \hat{h}^{\mu_\beta} D^A(\overline{t}^{\mu_\alpha}, t^{m_\zeta}) \tag{31}$$

The generalization of the implementation for the damped quadratic response function entailed generalizing the construction of the RHS for the response multiplier equations, the **G**-matrix contraction routines to handle two complex vectors, the **B**-matrix contraction routines to handle complex vectors from the left, the D^F density to handle complex amplitudes, and the D^A density to handle complex multipliers. The generalization of the latter also involved the on-the-fly evaluation of the double parts of the complex response vectors.

3. COMPUTATIONAL DETAILS

To illustrate the results, we examined the zinc tetrabenzoporphyrin (ZnTBP) complex in a planar geometry of D_{4h} symmetry, as sketched in Figure 1. A DFT-optimized geometry was obtained from ref 54 and reoptimized at the MP2/cc-pVTZ level of theory. The MCD spectra were computed with both resonant and damped response using a development version of TURBOMOLE 7.6.[39,55] The molecule was treated in its largest Abelian point group, D_{2h}, and the aug-cc-pVDZ basis set[56,57] was applied as orbital and auxiliary basis for H, C, and N. The energy-consistent pseudo potential (ECP) for Zn from Figgen et al.[58] was used in combination with the aug-cc-pVDZ-PP basis set[59] for both the orbital and auxiliary basis.

In the resonant response calculations, the MCD $\mathcal{B}$ terms were computed with the preexisting implementation,[10] whereas the $\mathcal{A}$ terms were obtained using our new contribution to the program.

Lorentzian broadening functions were applied to the resonant results such that

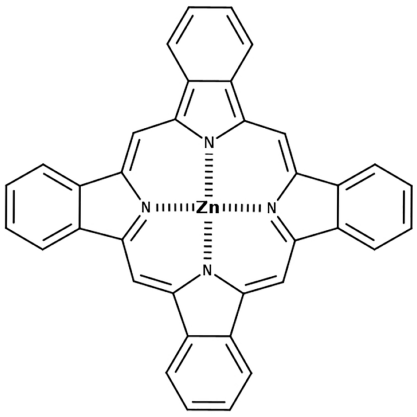


Figure 1. Zinc tetrabenzoporphyrine (ZnTBP).

$$g(\omega, \omega_j) = \frac{1}{\pi}\frac{\gamma}{(\omega - \omega_j)^2 + \gamma^2} \tag{32}$$

$$\frac{\partial g(\omega, \omega_j)}{\partial \omega} = -\frac{2}{\pi}\frac{(\omega - \omega_j)\gamma}{[(\omega - \omega_j)^2 + \gamma^2]^2} \tag{33}$$

By setting the half-width-at-half-maximum (HWHM) in the line shape functions equal to the damping factor applied in damped calculations, one obtains identical spectra from resonant and damped response, provided the latter is multiplied by a factor of π^{-1}. A damping factor of 4.5563×10^{-3} au (≈ 1000 cm^{-1}), as often used in the literature, was applied. The stick spectra were broadened with a HWHM of the same value, unless otherwise stated.

The 18 lowest electronically excited states were converged for resonant response: 8 of B_{2u}, 8 of B_{3u}, and 2 of B_{1u} symmetries. Oscillator strengths were calculated for all 18 states, while the MCD terms were calculated for the lowest 15 states. With the damped approach, the high-energy spectrum was initially built between 0.15 and 0.30 au with a distance of 0.01 au between the grid points. To obtain a higher resolution of some spectral features, additional grid points were calculated in the range 0.145−0.23 au, such that the separation between points in this interval was 0.005 au. The damped spectrum was drawn by the cubic interpolation of the grid points. The absorption and MCD spectra obtained from interpolation of the coarse grid are depicted in Figure S1. All raw data are available in the SI.

All calculations were carried out with the frozen core approximation. For the damped calculations, a convergence threshold of 1×10^{-4} was applied for both the linear equations and the numerical Laplace transformation; the qualitative results were found to be rather insensitive to the threshold. In the resonant case, the residuals of the eigenvalue and linear equations were converged below thresholds of 10^{-8} and 10^{-6}, respectively.

4. RESULTS AND DISCUSSION

4.1. Absorption and MCD Spectra. The ZnTBP molecule was chosen as an illustrative example due to the availability of an experimental MCD spectrum reaching energies as high as 8 eV (65 000 cm^{-1}),[60] covering what is referred to as the Q- (15 800−18 000 cm^{-1}), B- (23 500−29 000 cm^{-1}), N-, L-, and X-band (28 000−65 000 cm^{-1}) regions.[60,61] The experimental measurements were carried out in an argon matrix. It is noted that in the experiment, several nonequivalent sites in the Argon matrix together with crystal field (CF) splitting result in absorption and MCD spectra with a rich structure.[60] This is not reproduced by the calculations carried out in the gas phase. The Q- and B-band regions also reveal vibrational overtones in the experimental measurements.[60]

The simulated absorption and MCD spectra in the full energy range are depicted in Figure 2, where the broadened stick spectra cover the Q-, B-, N-, and L-bands, while the N-, L-, C-, and X-bands are covered by the damped results. An overlap between the resonant and the damped spectra ensures a complete description.

While the electronic transitions of the Q- and B-bands are well separated, the spectrum above 4 eV convolutes more close-lying states. Especially the C- and X-band regions contain a high density of states stemming from the large aromatic system of the TBP ligand. In the absorption spectrum of Figure 2, it is seen that the B-band has much higher intensity than the Q-band,

https://doi.org/10.1021/acs.jctc.3c00536
J. Chem. Theory Comput. 2023, 19, 5977−5987

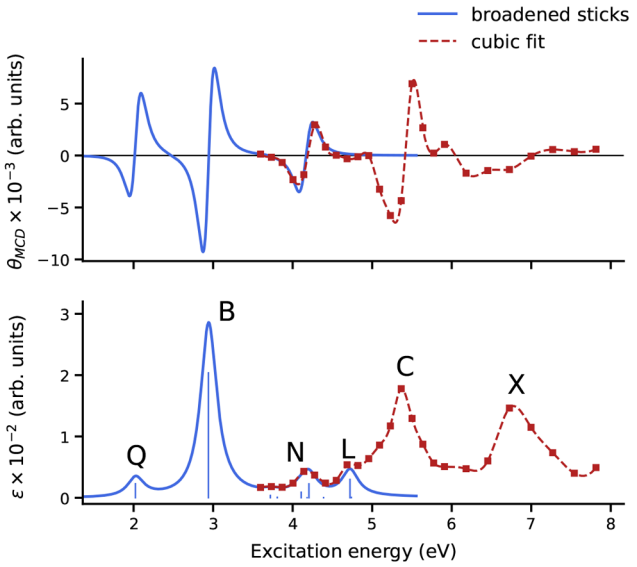


Figure 2. ZnTBP. Absorption (lower panel) and MCD (upper panel) spectra from standard (blue) and damped (red) response in the energy region 2−8 eV (15 000−65 000 cm^{-1}. Energies have been shifted by −0.349 eV (−2818 cm^{-1}).

consistent with previous findings.[60] The MCD spectrum is predominantly given by $\mathcal{A}$ terms, occurring in all bands except the X-band. The $\mathcal{A}$ terms are positive, as it can be seen from the negative wing at lower energies.

Experimental absorption and MCD spectra in three energy ranges are shown alongside the theoretical ones in Figures 3 and 4, respectively. The broadening factors of the stick spectra in the low- and midenergy panels have been reduced to the values

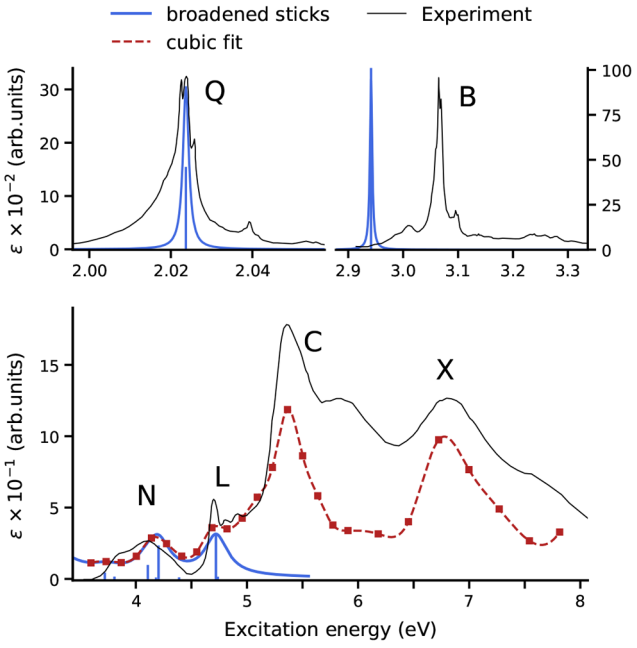


Figure 3. ZnTBP. Absorption spectra in three energy regions with experimental spectra from ref 60. Theoretical energies were shifted by −0.349 eV (−2818 cm^{-1}). HWHMs were 7 cm^{-1} (Q-band, upper left), 20 cm^{-1} (B-band, upper right), and 1000 cm^{-1} (N-X region, lower panel). The experimental spectra are presented without ε values.

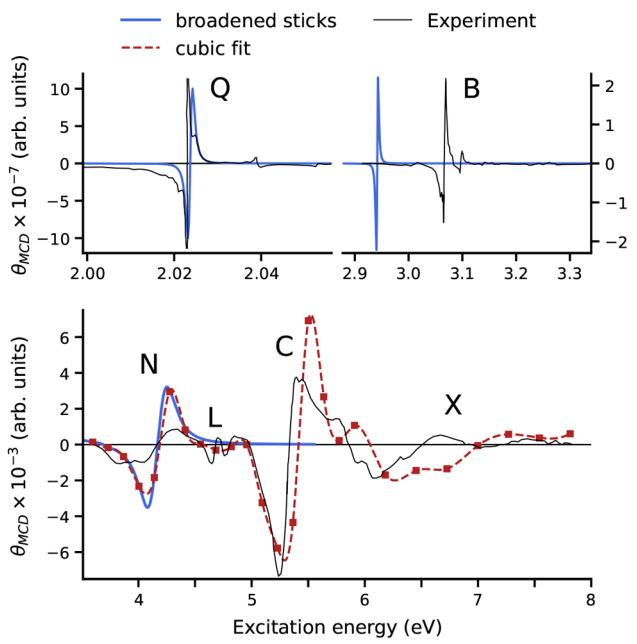


Figure 4. ZnTBP. MCD spectra in three energy regions with experimental spectra from ref 60. Theoretical energies have been shifted by −0.349 eV (−2818 cm^{-1}). HWHMs of 7 cm^{-1} (Q-band, upper left), 20 cm^{-1} (B-band, upper right), and 1000 cm^{-1} (N-X region, lower panel). The experimental spectra are presented without θ values.

indicated in the figure captions to be comparable to experiment which reports very high resolution of the Q- and B-bands.[60]

All theoretical spectra were red-shifted by 0.35 eV (2818 cm^{-1}) to align the first absorption peak with the corresponding peak of the major matrix site of the Q-band in the experimental absorption spectrum (Figure 3, upper left panel). The size of this shift is considered to be within what can be attributed to environmental effects, the deviation between computed vertical excitation energies and experimental band maxima in addition to the general overestimation of excitation energies within CC2.[62,63] The shift also aligns the maxima of the C- and X-bands in the high-energy region fairly well with experiment, although the separations between the spectral features in the simulated spectrum are slightly larger. Nevertheless, the features are reproduced well by our calculations. The MCD in the N-band region is, however, far more pronounced in the simulated spectrum. A better fit could be brought about by increasing the damping factor, i.e., the broadening of the spectrum.

The (shifted) B-band is located approximately 0.12 eV (994 cm^{-1}) to the red of the corresponding peak in the experiment, indicating that the computed energy gap between the first and second peak is too small. This is again within the error of CC2. If we align the spectra according to the B-band instead of the Q-band, the overall red shift is reduced to 0.23 eV (1825 cm^{-1}). However, this worsens the alignment of the high-energy region. Spectra shifted to align with the B-band are available in Figures S2 and S3 in the SI.

While the spectrum that convolutes the excitations underlying the X-band in the absorption spectrum is of similar intensity as the C-band, the MCD spectrum above 6 eV has a much lower intensity and is less rich in features. Looking at the lower panel in Figure 4, we see that a flattening of the spectrum in the X-band region is also observed experimentally. This observation suggests that this part of the spectrum is made of $\mathcal{B}$ terms, i.e., the convoluted states are nondegenerate, as the $\mathcal{B}$ terms are

https://doi.org/10.1021/acs.jctc.3c00536
J. Chem. Theory Comput. 2023, 19, 5977−5987

usually (much) smaller than the $\mathcal{A}$ terms, as previously mentioned. Figure 5 shows separate broadened $\mathcal{A}$- and $\mathcal{B}$-term spectra to illustrate this point. Note that the spectra are plotted on individual y axes. Interestingly, the $\mathcal{B}$ term spectrum reveals two oppositely signed terms of same magnitude between 4 and 4.5 eV (N-band region), a phenomenon referred to as a pseudo-$\mathcal{A}$ term.[64] It has here its origin in two ^1E_u states that contribute to the N-band which are only separated by ≈0.1 eV and coupled with a nonvanishing transition moment for the z component of the magnetic dipole operator.

In the experiment, it is reported that the zero-crossings of the MCD spectra do not fully coincide with the maxima in the absorption spectra, as is exhibited by true $\mathcal{A}$ terms.[60] The observed shift is attributed to symmetry-lowering effects arising from Jahn−Teller effects and CF splitting. The lowering of symmetry lifts the degeneracy between the pairs, which now instead appear as close-lying $\mathcal{B}$ terms of equal magnitude and opposite sign, i.e., as pseudo-$\mathcal{A}$ terms. Meanwhile, the splitting of the degenerate pair affects the absorption spectrum by resulting in two transitions with oscillator strengths that are likely to be different. This alters the position of the absorption maxima compared with the fully symmetric structure. Also, the superposition of nearby bands with different intensities in absorption and different ellipticities for MCD contributes to shifts between the maxima in the absorption and zero-crossings in the MCD spectra. All in all, one cannot, even at the most accurate theoretical level, expect a complete agreement with the experimental spectra used for comparison in the current work, since the experimental measurements do not reflect the perfectly symmetric molecule applied in the calculations. That the zero-crossing of the pseudo-$\mathcal{A}$ term feature under the (shifted) N-band (∼4.1 eV) in the calculated spectrum aligns almost perfectly with the experimental one is mostly coincidental.

It is also important to highlight that a nonphenomenological simulation of MCD shapes requires the inclusion of vibrational contributions.[15,65,66] It has been shown, for example, that in porphyrins the intensity of the absorption Q-band is enhanced by Herzberg−Teller vibrational effects, which shift the peak because the 0-0 transition is very weak and higher excited vibrational states absorb.[67] The same may hold true for MCD.

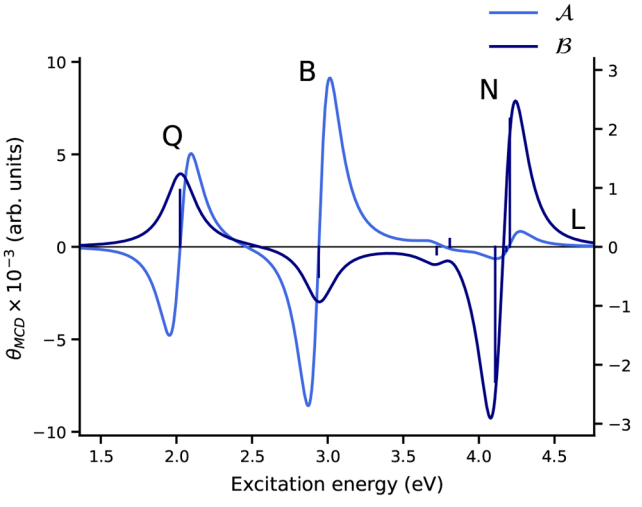


Figure 5. ZnTBP. MCD $\mathcal{A}$ (left y-axis, light blue) and $\mathcal{B}$ (right y-axis, navy) spectra. The sticks are $-\mathcal{B}$ terms scaled by a factor of 8 for visibility. Energies have been shifted by −0.349 eV (−2818 cm^{-1}).

Since this is a showcase example, and ZnTBP is a well-studied system,[54,68−71] we will not go further into analyzing the spectra.

4.2. Timings. For the evaluation of the time consumption of the two approaches, a damped calculation was carried out with a real frequency of 0.20 au and a damping factor of 4.5563×10^{-3} au. The frequency of 0.20 au lies in the upper L-band region, right "at the border" with the spectrally dense region. The resonance calculations were carried out for the lowest-energy degenerate set consisting of the first transitions of B_{2u} and B_{3u} symmetry. These calculations were carried out in shared-memory (OpenMP) parallel modality on 40 cores of two Intel Xeon Gold 6230 CPUs running at 2.1 GHz.

4.2.1. Calculation of the Quadratic Response Function. Table 1 summarizes the timings of a calculation of the quadratic response function with one complex frequency, as well as a calculation with only a real frequency. Two RHSs, two sets of linear equations, four types of densities, and two types of matrix contractions are involved; see the table for details. The ground state amplitudes, multipliers, and densities, the RHSs and linear solvers for the static magnetic perturbation, and the densities only perturbed by the magnetic dipole are all independent of the number of complex frequencies. The remaining components scale linearly.

It is clearly seen that the most time-consuming steps are the computation of the densities and matrix-vector contractions for building the quadratic response function: more than 70% of the total wall time was spent by those operations in both the real and complex cases. From the timings, it is observed that the RHSs and matrix-vector contractions take roughly twice as long for the complex response function, while the left- and right-hand transformations are faster when the frequency is complex. We note that the linear solver required nearly twice as many iterations for converging the response equations without a damping factor.

For an approximate evaluation of the time demand per frequency, we subtract from the total wall time the frequency-independent steps mentioned previously. This amounts to almost 35 h per complex frequency and 24 h per real frequency. There is thus only a 50% increase in the time consumption from regular to damped quadratic response, demonstrating the efficiency of the implementation of the damped response theory.

4.2.2. State-by-State Calculation. The timings from the resonant calculations are summarized in Table 2. Note that no timings for the CC equations are reported; in the setup, these were solved in a sequence of a CCS preoptimization, a quasi-linear CC2 preoptimization, and a final DIIS eigensolver for the nonlinear eigenvalue problem for $\mathbf{A}^{\text{eff}}_{SS}$.

In a resonant calculation, four sets of linear equations are solved, and their respective RHSs are built. For putting together the MCD ellipticity, 10 densities are computed and four matrix-vector contractions are carried out, see Table 2 for details. Besides the calculations related to just the ground state, only the RHS and linear solver for the magnetic-field-perturbed amplitudes are state-independent. All of the remaining steps scale linearly with the number of excited states.

Again, the computation of the property building blocks takes up a large part of the total wall time, amounting to 50% of the total wall time in the presented case. This is 20 percentage points less than observed for the quadratic response function and is a reflection of the substantial amount of additional linear equations that are required for the state-by-state approach,

https://doi.org/10.1021/acs.jctc.3c00536
J. Chem. Theory Comput. 2023, 19, 5977−5987

Table 1. ZnTBP: Timings from a Regular and Damped Quadratic Response Calculation with ω = 0.20 au and $\gamma = 4.5563 \times 10^{-3}$ au[a]

Type	Time (damped)	Time (regular)	Unit	#	Scaling
RHS (t^A)	363.58	175.00	sec/vec	9	3 + 6 n_{freq}
RHS ($\bar{t}^A$)	471.26	234.39	sec/vec	9	3 + 6 n_{freq}
RHTR (t^A)	37.69	62.59	sec/iter/vec	18	2 n_{RHS}
LHTR ($\bar{t}^A$)	37.22	42.28	sec/iter/vec	18	2 n_{RHS}
$D^\eta(\bar{t}, t^A)$ + int. for D^F	814.60	506.93	sec/dens	9	3 + 6 n_{freq}
$D^F(\bar{t}, t^A, t^B)$	0.24	0.11	sec/dens	18	18 n_{freq}
$D^\xi(\bar{t}^A, t)$ + int. for D^A	1392.87	806.60	sec/dens	9	3 + 6 n_{freq}
$D^A(\bar{t}^A, t^B)$	1651.43	1226.67	sec/dens	36	36 n_{freq}
$\bar{t}^A$ **B** $t^B t^C$	1114.67	586.21	sec/contr	18	18 n_{freq}
G $t^A t^B t^C$	123.83	67.67	sec/contr	6	6 n_{freq}

[a]Data for right-hand sides (RHS), right- and left-hand transformations (RHTR, LHTR), densities, and contractions, along with the number of vectors, densities, or contractions of the given "Type", as well as the scaling of the number of "Types" with the number of frequencies, n_{freq}, or RHSs, n_{RHS}. Times are normalized over all symmetries and/or permutations; "int." = intermediate(s).

Table 2. ZnTBP: Timings from a Resonant Response Calculation of the MCD of the First Degenerate Set of Excited States[a]

Type	Time	Unit	#
RHS ($\bar{M}_j$)	115.44	sec/vec	2
RHS (t^A)	194.25	sec/vec	7
RHS (E_j^A)	956.55	sec/vec	8
RHS ($\bar{E}_j^A$)	309.58	sec/vec	4
LHTR ($\bar{M}_j$)	53.37	sec/iter/vec	2
RHTR (t^A)	80.61	sec/iter/vec	7
RHTR (E_j^A)	360.03	sec/iter/vec	12
LHTR ($\bar{E}_j^A$)	25.45	sec/iter/vec	8
$D^\xi(\bar{E}_j, t)$ + int. for $D^A(E_j, t^A)$	47.70	sec/dens	2
$D^\xi(\bar{M}_j, t)$ + int. for $D^A(\bar{M}_j, t^A)$	50.10	sec/dens	2
$D^\eta(\bar{t}, E_j^A)$	1381.28	sec/dens	8
$D^\eta(\bar{t}, E_j)$ + int. for $D^F(\bar{t}, E_j, t^A)$	85.80	sec/dens	2
$D^\eta(\bar{t}, t^A)$ + int. for $D^F(\bar{t}, E_j, t^A)$	691.89	sec/dens	7
$D^A(\bar{E}_j, t^A)$	697.50	sec/dens	4
$D^A(\bar{M}_j, t^A)$	699.90	sec/dens	8
$D^A(\bar{E}_j, E_{j'})$	103.20	sec/dens	2
$D^F(\bar{t}, E_j, t^A)$	0.11	sec/dens	8
$D^\xi(\bar{E}_j^A, t)$	1040.70	sec/dens	4
$\bar{M}_j$**B** $t^A t^B$	428.86	sec/contr	4
F $E_j^A t^B$	530.28	sec/contr	8
$\bar{E}_j$**B** $t^A E_{j'}$	233.74	sec/contr	6
G $E_j t^A t^B$	105.50	sec/contr	4

[a]Data for right hand sides (RHS), right- and left hand transformations (RHTR, LHTR), densities, and contractions, along with the number of vectors, densities, or contractions of the given "Type". Times are normalized over all symmetries and/or permutations. "int." = intermediate(s).

besides, of course, the lower computational cost and scaling of the densities.

The time required per resonant state was approximately 9 h. This measure represents a lower limit for the cost of the resonant approach. As the number of requested states increases, so will the number of iterations required before convergence is reached in the eigen and linear solvers.

5. CONCLUDING REMARKS

We have presented the implementation of the MCD $\mathcal{A}$ term and of the quadratic response function for real and complex frequencies to include the damped response case for MCD at the (RI-)CC2 level of theory in Turbomole.[39,55] We applied them to the highly symmetric ZnTBP molecule to show how a combination of resonant and damped response theory can be used to efficiently compute MCD spectra for relatively large chromophores. By combining the resonant and damped response results, the absorption and MCD spectra have been simulated in the region 2−8 eV (16 000−65 000 cm^{-1}) and compared to experimental data from the literature. Good agreement was found between the theoretical and experimental spectra, where the errors of the computed excitation energies were assigned to the neglect of environmental effects, deviations between vertical excitations, and band maxima, as well as the general error of CC2.

Timings have been reported for a resonant calculation of a set of degenerate states and a damped calculation with one complex frequency. It was found that the computation of the building blocks of the final property is by far the most time-consuming for both the resonant and damped case, although the former spends three times the amount of percentage points on the construction of RHSs compared to the damped approach. The break-even point between resonant and damped calculations is approximately hit when the number of states exceeds four times the number of grid points needed to cover the same frequency range.

The final recommendation for the application of our procedure is to use the resonant approach for the low-energy region of the MCD spectrum, where the density of states is typically low, and the resonant approach is expected to be the most efficient one. The spectrum is then extended to higher energies by producing a grid of cross sections with damped calculations. An overlap with the low-energy spectrum is advised for a complete description of the spectrum. The damping factor can be chosen based on the resolution of an experimental spectrum. If no experiment is available, or if no resolution is reported, a factor of 1000 cm^{-1} typically gives a reasonable theoretical spectrum. The step size should roughly correspond to the damping factor. In the current work, this was the case in regions with stronger spectral features, while less rich regions were treated with a step of twice this size.

For the damped spectrum, an initial calculation with a larger damping factor and a smaller basis can be used to identify important regions in the spectrum that need a denser grid or a smaller damping factor. At least, it is beneficial to first produce a coarse grid and then supplement it with more points in regions in which more pronounced spectral features are expected.

https://doi.org/10.1021/acs.jctc.3c00536
J. Chem. Theory Comput. 2023, 19, 5977−5987

Furthermore, it should be exploited that the damped approach can be used at any frequency interval (including the X-ray regime), meaning that several batches of, e.g., four complex frequencies each can be carried out simultaneously, thereby scanning a large frequency range in a (relatively) short amount of time. It is our experience that a cubic spline provides a good interpolation of the data points with respect to reproducing a broadened stick spectrum and avoiding an overfit of the parameters.

■ ASSOCIATED CONTENT

Supporting Information

The Supporting Information is available free of charge at https://pubs.acs.org/doi/10.1021/acs.jctc.3c00536.

Cartesian coordinates, numerical data, additional figures, generalization of response multipliers equations, reduced space residual minimization, **G**-matrix contractions (PDF)

■ AUTHOR INFORMATION

Corresponding Authors

Josefine H. Andersen − *Department of Chemistry, Technical University of Denmark, DK-2800 Kongens Lyngby, Denmark;* orcid.org/0000-0002-0534-7463; Email: johvan@kemi.dtu.dk

Sonia Coriani − *Department of Chemistry, Technical University of Denmark, DK-2800 Kongens Lyngby, Denmark;* orcid.org/0000-0002-4487-897X; Email: soco@kemi.dtu.dk

Christof Hättig − *Arbeitsgruppe Quantenchemie, Ruhr-Universität Bochum, D-44780 Bochum, Germany;* orcid.org/0000-0002-5752-2710; Email: christof.haettig@rub.de

Complete contact information is available at: https://pubs.acs.org/10.1021/acs.jctc.3c00536

Notes

The authors declare no competing financial interest.

■ ACKNOWLEDGMENTS

JHA and SC acknowledge financial support from the Independent Research Fund Denmark-Natural Sciences, Research Project 2 - grant no. 7014-00258B. CH acknowledges financial support from the Deutsche Forschungsgemeinschaft through project 10-1.

■ REFERENCES

(1) Mason, W. R. *A Practical Guide to Magnetic Circular Dichroism Spectroscopy*; John Wiley & Sons, Inc., 2007; pp 1−223.

(2) Keiderling, T. A. Observation of magnetic vibrational circular dichroism. *J. Chem. Phys.* **1981**, *75*, 3639−3641.

(3) Cao, J.; Ye, L.; He, D.; Zheng, X.; Mukamel, S. Magnet-Free Time-Resolved Magnetic Circular Dichroism with Pulsed Vector Beams. *J. Phys. Chem. Lett.* **2022**, *13*, 11300−11306.

(4) Han, B.; Gao, X.; Lv, J.; Tang, Z. Magnetic Circular Dichroism in Nanomaterials: New Opportunity in Understanding and Modulation of Excitonic and Plasmonic Resonances. *Adv. Mater.* **2020**, *32*, 1801491.

(5) Mason, W. R. In *Comprehensive Coordination Chemistry II. Vol. 2: Fundamentals: Physical Methods, Theoretical Analysis, and Case Studies*; Lever, A. B. P., Ed.; Elsevier, 2003; Vol. 2, Chapter 2.25.

(6) Solomon, E. I.; Neidig, M. L.; Schenk, G. In *Comprehensive Coordination Chemistry II. Vol. 2: Fundamentals: Physical Methods, Theoretical Analysis, and Case Studies*; Lever, A. B. P., Ed.; Elsevier, 2003; Vol. 2, Chapter 2.26.

(7) Christiansen, O.; Jørgensen, P.; Hättig, C. Response functions from Fourier component variational perturbation theory applied to a time-averaged quasienergy. *Int. J. Quantum Chem.* **1998**, *68*, 1−52.

(8) Fedotov, D. A.; Scott, M.; Scheurer, M.; Rehn, D. R.; Dreuw, A.; Coriani, S. Magnetic circular dichroism within the algebraic diagrammatic construction scheme of the polarization propagator up to third order. *J. Chem. Phys.* **2022**, *157*, 174109.

(9) Faber, R.; Ghidinelli, S.; Hättig, C.; Coriani, S. Magnetic circular dichroism spectra from resonant and damped coupled cluster response theory. *J. Chem. Phys.* **2020**, *153*, 114105.

(10) Khani, S. K.; Faber, R.; Santoro, F.; Hättig, C.; Coriani, S. UV Absorption and Magnetic Circular Dichroism Spectra of Purine, Adenine, and Guanine: A Coupled Cluster Study in Vacuo and in Aqueous Solution. *J. Chem. Theory Comput.* **2019**, *15*, 1242−1254.

(11) Sun, S.; Williams-Young, D.; Li, X. An ab Initio Linear Response Method for Computing Magnetic Circular Dichroism Spectra with Nonperturbative Treatment of Magnetic Field. *J. Chem. Theory Comput.* **2019**, *15*, 3162−3169.

(12) Sun, S.; Beck, R. A.; Williams-Young, D.; Li, X. Simulating Magnetic Circular Dichroism Spectra with Real-Time Time-Dependent Density Functional Theory in Gauge Including Atomic Orbitals. *J. Chem. Theory Comput.* **2019**, *15*, 6824−6831.

(13) Pausch, A.; Holzer, C.; Klopper, W. Efficient Calculation of Magnetic Circular Dichroism Spectra Using Spin-Noncollinear Linear-Response Time-Dependent Density Functional Theory in Finite Magnetic Fields. *J. Chem. Theory Comput.* **2022**, *18*, 3747−3758.

(14) Sun, S.; Li, X. Relativistic Effects in Magnetic Circular Dichroism: Restricted Magnetic Balance and Temperature Dependence. *J. Chem. Theory Comput.* **2020**, *16*, 4533−4542.

(15) Foglia, N.; De Souza, B.; Maganas, D.; Neese, F. Including vibrational effects in magnetic circular dichroism spectrum calculations in the framework of excited state dynamics. *J. Chem. Phys.* **2023**, *158*, 154108.

(16) Norman, P. A perspective on non resonant and resonant electronic response theory for time-dependent molecular properties. *Phys. Chem. Chem. Phys.* **2011**, *13*, 20519−20535.

(17) Kristensen, K.; Kauczor, J.; Kjærgaard, T.; Jørgensen, P. Quasienergy formulation of damped response theory. *J. Chem. Phys.* **2009**, *131*, 044112.

(18) Helgaker, T.; Coriani, S.; Jørgensen, P.; Kristensen, K.; Olsen, J.; Ruud, K. Recent Advances in Wave Function Based Methods of Molecular-Property Calculations. *Chem. Rev.* **2012**, *112*, 543−631.

(19) Fedotov, D. A.; Coriani, S.; Hättig, C. Damped (linear) response theory within the resolution-of-identity coupled cluster singles and approximate doubles (RI-CC2) method. *J. Chem. Phys.* **2021**, *154*, 124110.

(20) Ekström, U.; Norman, P.; Carravetta, V.; Ågren, H. Polarization Propagator for X-Ray Spectra. *Phys. Rev. Lett.* **2006**, *97*, 143001.

(21) Ekström, U.; Norman, P. X-ray absorption spectra from the resonant-convergent first-order polarization propagator approach. *Phys. Rev. A* **2006**, *74*, 042722.

(22) Jiemchooroj, A.; Norman, P. Electronic circular dichroism spectra from the complex polarization propagator. *J. Chem. Phys.* **2007**, *126*, 134102.

(23) Coriani, S.; Christiansen, O.; Fransson, T.; Norman, P. Coupled-cluster response theory for near-edge x-ray-absorption fine structure of atoms and molecules. *Phys. Rev. A* **2012**, *85*, 022507.

(24) Andersen, J. H.; Nanda, K. D.; Krylov, A. I.; Coriani, S. Probing Molecular Chirality of Ground and Electronically Excited States in the UV−vis and X-ray Regimes: An EOM-CCSD Study. *J. Chem. Theory Comput.* **2022**, *18*, 1748−1764.

(25) Jiemchooroj, A.; Sernelius, B. E.; Norman, P. C_6 dipole-dipole dispersion coefficients for the *n*-alkanes: Test of an additivity procedure. *Phys. Rev. A* **2004**, *69*, 044701.

(26) Coriani, S.; Fransson, T.; Christiansen, O.; Norman, P. Asymmetric-Lanczos-Chain-Driven Implementation of Electronic

Resonance Convergent Coupled-Cluster Linear Response Theory. *J. Chem. Theory Comput.* **2012**, *8*, 1616−1628.
(27) Fransson, T.; Rehn, D. R.; Dreuw, A.; Norman, P. Static polarizabilities and C_6 dispersion coefficients using the algebraic-diagrammatic construction scheme for the complex polarization propagator. *J. Chem. Phys.* **2017**, *146*, 094301.
(28) Solheim, H.; Ruud, K.; Coriani, S.; Norman, P. Complex polarization propagator calculations of magnetic circular dichroism spectra. *J. Chem. Phys.* **2008**, *128*, 094103.
(29) Vaara, J.; Rizzo, A.; Kauczor, J.; Norman, P.; Coriani, S. Nuclear spin circular dichroism. *J. Chem. Phys.* **2014**, *140*, 134103.
(30) Cukras, J.; Kauczor, J.; Norman, P.; Rizzo, A.; Rikken, G. L. J. A.; Coriani, S. A complex-polarization-propagator protocol for magneto-chiral axial dichroism and birefringence dispersion. *Phys. Chem. Chem. Phys.* **2016**, *18*, 13267−13279.
(31) Rehn, D. R.; Dreuw, A.; Norman, P. Resonant Inelastic X-ray Scattering Amplitudes and Cross Sections in the Algebraic Diagrammatic Construction/Intermediate State Representation (ADC/ISR) Approach. *J. Chem. Theory Comput.* **2017**, *13*, 5552−5559.
(32) Faber, R.; Coriani, S. Resonant Inelastic X-ray Scattering and Nonesonant X-ray Emission Spectra from Coupled-Cluster (Damped) Response Theory. *J. Chem. Theory Comput.* **2019**, *15*, 520−528.
(33) Faber, R.; Coriani, S. Core−valence-separated coupled-cluster-singles-and-doubles complex-polarization-propagator approach to X-ray spectroscopies. *Phys. Chem. Chem. Phys.* **2020**, *22*, 2642−2647.
(34) Nanda, K. D.; Vidal, M. L.; Faber, R.; Coriani, S.; Krylov, A. I. How to stay out of trouble in RIXS calculations within equation-of-motion coupled-cluster damped response theory? Safe hitchhiking in the excitation manifold by means of core−valence separation. *Phys. Chem. Chem. Phys.* **2020**, *22*, 2629−2641.
(35) Schnack-Petersen, A. K.; Moitra, T.; Folkestad, S. D.; Coriani, S. New Implementation of an Equation-of-Motion Coupled-Cluster Damped-Response Framework with Illustrative Applications to Resonant Inelastic X-ray Scattering. *J. Phys. Chem. A* **2023**, *127*, 1775−1793.
(36) Kristensen, K.; Kauczor, J.; Thorvaldsen, A. J.; Jørgensen, P.; Kjærgaard, T.; Rizzo, A. Damped response theory description of two-photon absorption. *J. Chem. Phys.* **2011**, *134*, 214104.
(37) Fahleson, T.; Ågren, H.; Norman, P. A Polarization Propagator for Nonlinear X-ray Spectroscopies. *J. Phys. Chem. Lett.* **2016**, *7*, 1991−1995.
(38) Hu, Z.; Autschbach, J.; Jensen, L. Simulating Third-Order Nonlinear Optical Properties Using Damped Cubic Response Theory within Time-Dependent Density Functional Theory. *J. Chem. Theory Comput.* **2016**, *12*, 1294−1304.
(39) Balasubramani, S. G.; Chen, G. P.; Coriani, S.; Diedenhofen, M.; Frank, M. S.; Franzke, Y. J.; Furche, F.; Grotjahn, R.; Harding, M. E.; Hättig, C.; Hellweg, A.; Helmich-Paris, B.; Holzer, C.; Huniar, U.; Kaupp, M.; Marefat Khah, A.; Karbalaei Khani, S.; Müller, T.; Mack, F.; Nguyen, B. D.; Parker, S. M.; Perlt, E.; Rappoport, D.; Reiter, K.; Roy, S.; Rückert, M.; Schmitz, G.; Sierka, M.; Tapavicza, E.; Tew, D. P.; van Wüllen, C.; Voora, V. K.; Weigend, F.; Wodyński, A.; Yu, J. M. TURBOMOLE: Modular program suite for ab initio quantum-chemical and condensed-matter simulations. *J. Chem. Phys.* **2020**, *152*, 184107.
(40) Kjærgaard, T.; Kristensen, K.; Kauczor, J.; Jørgensen, P.; Coriani, S.; Thorvaldsen, A. J. Comparison of standard and damped response formulations of magnetic circular dichroism. *J. Chem. Phys.* **2011**, *135*, 024112.
(41) Buckingham, A. D.; Stephens, P. J. Magnetic Optical Activity. *Annu. Rev. Phys. Chem.* **1966**, *17*, 399−432.
(42) Barron, L. D. *Molecular Light Scattering and Optical Activity*, 2nd ed.; Cambridge University Press, 2004.
(43) Coriani, S.; Jørgensen, P.; Rizzo, A.; Ruud, K.; Olsen, J. Ab initio determinations of magnetic circular dichroism. *Chem. Phys. Lett.* **1999**, *300*, 61−68.
(44) Coriani, S.; Hättig, C.; Jørgensen, P.; Helgaker, T. Gauge-origin independent magneto-optical activity within coupled cluster response theory. *J. Chem. Phys.* **2000**, *113*, 3561−3572.
(45) Krykunov, M.; Seth, M.; Ziegler, T.; Autschbach, J. Calculation of the magnetic circular dichroism B term from the imaginary part of the Verdet constant using damped time-dependent density functional theory. *J. Chem. Phys.* **2007**, *127*, 244102.
(46) Kjærgaard, T.; Jørgensen, P.; Thorvaldsen, A. J.; Sałek, P.; Coriani, S. Gauge-Origin Independent Formulation and Implementation of Magneto-Optical Activity within Atomic-Orbital-Density Based Hartree-Fock and Kohn-Sham Response Theories. *J. Chem. Theory Comput.* **2009**, *5*, 1997−2020.
(47) Hättig, C.; Köhn, A. Transition moments and excited-state first-order properties in the coupled-cluster model CC2 using the resolution-of-the-identity approximation. *J. Chem. Phys.* **2002**, *117*, 6939−6951.
(48) Pabst, M.; Köhn, A. Implementation of transition moments between excited states in the approximate coupled-cluster singles and doubles model. *J. Chem. Phys.* **2008**, *129*, 214101.
(49) Christiansen, O.; Koch, H.; Jørgensen, P. The second-order approximate coupled cluster singles and doubles model CC2. *Chem. Phys. Lett.* **1995**, *243*, 409−418.
(50) Helmich-Paris, B.; Hättig, C.; van Wüllen, C. Spin-Free CC2 Implementation of Induced Transitions between Singlet Ground and Triplet Excited States. *J. Chem. Theory Comput.* **2016**, *12*, 1892−1904.
(51) Solheim, H.; Ruud, K.; Coriani, S.; Norman, P. The A and B Terms of Magnetic Circular Dichroism Revisited. *J. Phys. Chem. A* **2008**, *112*, 9615−9618.
(52) Kjærgaard, T.; Coriani, S.; Ruud, K. Ab initio calculation of magnetic circular dichroism. *WIREs Comput. Mol. Sci.* **2012**, *2*, 443−455.
(53) Friese, D. H.; Winter, N. O. C.; Balzerowski, P.; Schwan, R.; Hättig, C. Large scale polarizability calculations using the approximate coupled cluster model CC2 and MP2 combined with the resolution-of-the-identity approximation. *J. Chem. Phys.* **2012**, *136*, 174106.
(54) Nguyen, K. A.; Pachter, R. Ground state electronic structures and spectra of zinc complexes of porphyrin, tetraazaporphyrin, tetrabenzoporphyrin, and phthalocyanine: A density functional theory study. *J. Chem. Phys.* **2001**, *114*, 10757−10767.
(55) Franzke, Y. J.; Holzer, C.; Andersen, J. H.; Begušić, T.; Bruder, F.; Coriani, S.; Della Sala, F.; Fabiano, E.; Fedotov, D. A.; Fürst, S.; Gillhuber, S.; Grotjahn, R.; Kaupp, M.; Kehry, M.; Krstić, M.; Mack, F.; Majumdar, S.; Nguyen, B. D.; Parker, S. M.; Pauly, F.; Pausch, A.; Perlt, E.; Phun, G. S.; Rajabi, A.; Rappoport, D.; Samal, B.; Schrader, T.; Sharma, M.; Tapavicza, E.; Treß, R. S.; Voora, V.; Wodyński, A.; Yu, J. M.; Zerulla, B.; Furche, F.; Hättig, C.; Sierka, M.; Tew, D. P.; Weigend, F. TURBOMOLE: Today and Tomorrow. *J. Chem. Theory Comput.* **2023**.
(56) Dunning, T. H. Gaussian basis sets for use in correlated molecular calculations. I. The atoms boron through neon and hydrogen. *J. Chem. Phys.* **1989**, *90*, 1007−1023.
(57) Kendall, R. A.; Dunning, T. H.; Harrison, R. J. Electron affinities of the first-row atoms revisited. Systematic basis sets and wave functions. *J. Chem. Phys.* **1992**, *96*, 6796−6806.
(58) Figgen, D.; Rauhut, G.; Dolg, M.; Stoll, H. Energy-consistent pseudopotentials for group 11 and 12 atoms: adjustment to multi-configuration Dirac−Hartree−Fock data. *Chem. Phys.* **2005**, *311*, 227−244.
(59) Peterson, K. A.; Puzzarini, C. Systematically convergent basis sets for transition metals. II. Pseudopotential-based correlation consistent basis sets for the group 11 (Cu, Ag, Au) and 12 (Zn, Cd, Hg) elements. *Theor. Chem. Acc.* **2005**, *114*, 283−296.
(60) VanCott, T. C.; Koralewski, M.; Metcalf, D. H.; Schatz, P. N.; Williamson, B. E. Magnetooptical spectroscopy of zinc tetrabenzoporphyrin in an argon matrix. *J. Phys. Chem.* **1993**, *97*, 7417−7426.
(61) Edwards, L.; Gouterman, M.; Rose, C. B. Synthesis and vapor spectrum of zinc tetrabenzporphine. *J. Am. Chem. Soc.* **1976**, *98*, 7638−7641.
(62) Bai, S.; Mansour, R.; Stojanović, L.; Toldo, J. M.; Barbatti, M. On the origin of the shift between vertical excitation and band maximum in molecular photoabsorption. *J. Mol. Model.* **2020**, *26*, 107−115.

https://doi.org/10.1021/acs.jctc.3c00536
J. Chem. Theory Comput. 2023, 19, 5977−5987

(63) Winter, N. O. C.; Graf, N. K.; Leutwyler, S.; Hättig, C. Benchmarks for 0−0 transitions of aromatic organic molecules: DFT/B3LYP, ADC(2), CC2, SOS-CC2 and SCS-CC2 compared to high-resolution gas-phase data. *Phys. Chem. Chem. Phys.* **2013**, *15*, 6623−6630.
(64) Piepho, S. B.; Schatz, P. N. *Group theory in spectroscopy: with applications to magnetic circular dichroism*; Wiley-Interscience, 1983; Vol. *1*.
(65) Lin, N.; Solheim, H.; Zhao, X.; Santoro, F.; Ruud, K. First Principles Studies of the Vibrationally Resolved Magnetic Circular Dichroism Spectra of Biphenylene. *J. Chem. Theory Comput.* **2013**, *9*, 1557−1567.
(66) Kaminský, J.; Chalupský, J.; Štěpánek, P.; Kříž, J.; Bouř, P. Vibrational Structure in Magnetic Circular Dichroism Spectra of Polycyclic Aromatic Hydrocarbons. *J. Phys. Chem. A* **2017**, *121*, 9064−9073.
(67) Santoro, F.; Lami, A.; Improta, R.; Bloino, J.; Barone, V. Effective method for the computation of optical spectra of large molecules at finite temperature including the Duschinsky and Herzberg−Teller effect: The Qx band of porphyrin as a case study. *J. Chem. Phys.* **2008**, *128*, 224311.
(68) Zhou, X.; Ren, A.-M.; Feng, J.-K.; Liu, X.-J. Theoretical studies on the one- and two-photon absorption of tetrabenzoporphyrins and phthalocyanines. *Can. J. Chem.* **2004**, *82*, 19−26.
(69) Guo, M.; He, R.; Dai, Y.; Shen, W.; Li, M.; Zhu, C.; Lin, S. H. Franck-Condon simulation of vibrationally resolved optical spectra for zinc complexes of phthalocyanine and tetrabenzoporphyrin including the Duschinsky and Herzberg-Teller effects. *J. Chem. Phys.* **2012**, *136*.
(70) Theisen, R. F.; Huang, L.; Fleetham, T.; Adams, J. B.; Li, J. Ground and excited states of zinc phthalocyanine, zinc tetrabenzoporphyrin, and azaporphyrin analogs using DFT and TDDFT with Franck-Condon analysis. *J. Chem. Phys.* **2015**, *142*, 094310.
(71) Eroshin, A. V.; Otlyotov, A. A.; Kuzmin, I. A.; Stuzhin, P. A.; Zhabanov, Y. A. DFT Study of the Molecular and Electronic Structure of Metal-Free Tetrabenzoporphyrin and Its Metal Complexes with Zn, Cd, Al, Ga, In. *Int. J. Mol. Sci.* **2022**, *23*, 939.

Recommended by ACS

Reduced Scaling Real-Time Coupled Cluster Theory
Benjamin G. Peyton, T. Daniel Crawford, *et al.*
OCTOBER 02, 2023
THE JOURNAL OF PHYSICAL CHEMISTRY A
READ

Vertical Ionization Potentials and Electron Affinities at the Double-Hybrid Density Functional Level
Dávid Mester and Mihály Kállay
JUNE 16, 2023
JOURNAL OF CHEMICAL THEORY AND COMPUTATION
READ

Real-Time Equation-of-Motion Coupled-Cluster Cumulant Green's Function Method: Heterogeneous Parallel Implementation Based on the Tensor Algebra for Many-...
Himadri Pathak, Karol Kowalski, *et al.*
APRIL 05, 2023
JOURNAL OF CHEMICAL THEORY AND COMPUTATION
READ

Transition Moments for STEOM-CCSD with Core Triples
Megan Simons and Devin A. Matthews
JULY 12, 2023
JOURNAL OF CHEMICAL THEORY AND COMPUTATION
READ

Get More Suggestions >

https://doi.org/10.1021/acs.jctc.3c00536
J. Chem. Theory Comput. 2023, 19, 5977−5987